coatings

MDPI

Article

Surface-Termination Groups' Tuning to Improve the Lithium-Ion-Storage Performance of $Ti_3C_2T_x$ MXene

Andong Li [1,†], Xiaotong Wang [2,†], Jingjing Chen [1,*], Chenlong Dong [2], Dajian Wang [2] and Zhiyong Mao [2,*]

[1] School of Science, Tianjin University of Technology, Tianjin 300384, China; lad15822305017@163.com
[2] School of Materials Science and Engineering, Tianjin University of Technology, Tianjin 300384, China; amberwxt@163.com (X.W.); dongchenlong@email.tiut.edu.cn (C.D.); djwang@tjut.edu.cn (D.W.)
* Correspondence: cj313313@email.tjut.edu.cn (J.C.); mzhy1984@163.com (Z.M.)
† These authors contributed equally to this work.

Abstract: Two-dimensional transition metal carbides/carbonitrides (MXenes) have broad application prospects in the field of energy storage due to their abundant surface functional groups, tunable interlayer spacing, and excellent electrical conductivity. However, the kinetics of Li-ion intercalation/deintercalation between MXene layers is slow, and the stacking between nanosheets due to long cycling reduces the structural stability and battery safety. Herein, we prepare and tune surface-termination groups of $Ti_3C_2T_x$ MXene by chemical exfoliation and low-temperature annealing methods. The types of functional groups on the surface of the material are optimized by the substitution of oxygen to some -F functional groups on the surface. The optimized $Ti_3C_2T_x$ MXene material exhibits a reversible lithium-ion-storage specific capacity of 444.1 mAh g^{-1} after 200 cycles at a current density of 0.1 A g^{-1}. The increased of -O functional groups can increase the diffusion rate of Li^+, promote the transport of electrons, and accelerate the kinetics of the electrode reaction, thereby improving the performance of lithium-ion storage.

Keywords: $Ti_3C_2T_x$ MXene; chemical exfoliation; lithium-ion storage

Citation: Li, A.; Wang, X.; Chen, J.; Dong, C.; Wang, D.; Mao, Z. Surface-Termination Groups' Tuning to Improve the Lithium-Ion-Storage Performance of $Ti_3C_2T_x$ MXene. *Coatings* **2022**, *12*, 1005. https://doi.org/10.3390/coatings12071005

Academic Editor: Emerson Coy

Received: 22 June 2022
Accepted: 15 July 2022
Published: 17 July 2022

1. Introduction

With the rapid development of the global economy, fuel consumption, and increasingly serious environmental problems, there is an urgent need to develop clean, efficient, and sustainable energy-storage and -conversion technologies [1,2]. Based on the working principle of electrochemical energy conversion and storage, alkali metal-ion batteries are considered as the most promising next-generation energy-storage devices, which can effectively promote the development of sustainable energy and reduce environmental pollution [3]. At present, the demand for high-energy-density and high-power-density electrochemical energy-storage devices is increasing, and the demand for long-cycle stability and low-cost electrode materials is particularly urgent. Among the numerous nanomaterials, two-dimensional (2D) materials have broad application prospects in alkali metal-ion batteries due to their unique layered structure [4]. The layered structure can provide abundant channels for ion diffusion, accelerate the ion-diffusion process, and facilitate the realization of fast electron transport within the atomic layer. In addition, the layered structure can buffer the volume change during charging and discharging and improve the contact stability of the material [5].

As a new type of 2D layered transition metal carbides, MXenes have received extensive attention since the successful acquisition of MXenes in the MAX phase [6–12]. The general formula is $M_{n+1}X_nT_x$ (n = 1–3), where M represents an early transition metal (Ti, V, Cr, Nb, etc.), X is C or N, and T is the surface terminus [8,13–17]. MXenes have abundant surface functional groups and have been widely studied as electrodes for Li/Na-ion batteries [18–20] and supercapacitors [21–24] due to their good electrical and ionic conductivity.

Since Gogotsi et al. [9] obtained 2D $Ti_3C_2T_x$ materials by selective HF etching of Ti_3AlC_2 compounds in 2011, the family of 2D transition metal carbides, nitrides, and carbonitrides (MXenes) has gradually expanded. After more than ten years of research, dozens of MXenes materials have been successfully prepared. Pure-phase MXenes exhibit similar metallicity to their precursor MAX, but theory predicts that they could also be semiconductors [25] or topological insulators [26]. In general, the electronic structure of MXene is affected by the following three aspects: chemical composition (elemental species of M, X, T), crystal structure, and location of functional groups. Therefore, surface-controlled functionalization modification has become a common method to improve the physicochemical properties of MXene and endow its composites with new functions. In addition, MXene not only has the performance of traditional two-dimensional materials, but also has energy storage, good electrical conductivity, and self-lubricating properties, etc., showing great application potential in many fields such as energy storage, catalysis, and tribology. However, the current understanding of the structure and properties of MXene is still limited, and a lot of research work is still needed to fully understand the various properties of MXene.

The preparation of MXenes is usually performed by etching the MAX phase by the HF or LiF/HCl system. After etching, -O, -F and -OH functional groups will be introduced on the surface of the material. The Li ions penetrate and store the inner MXene sheet with a theoretical capacity of 447.8 mAh g^{-1} [27]. However, the -F termination groups usually reduce the initial discharge capacity and cycling stability due to poor electrode/electrolyte interface. The introduction of fluorine end-groups also increases the interface resistance between the electrode and the electrolyte. This further reduces the lithium-storage performance and cycle stability of the electrode [12,28,29]. In addition, MXenes bulks have many problems such as easy stacking of sheets, poor mechanical strength, and easy oxidation during the preparation process, which lead to the blockage of electron-/ion-transport channels and the collapse of the microstructure. Therefore, it is necessary to improve MXenes-based energy-storage materials from the perspective of surface functional groups and bulk microstructure. In terms of bulk microstructure, Lian et al. used KOH solution to exfoliate $Ti_3C_2T_x$ nanosheets, and the interlayer spacing of the exfoliated $Ti_3C_2T_x$ nanosheets expanded, thereby accelerating ion transport [30]. In terms of surface functional groups, Ahmed et al. used H_2O_2 to treat Ti_2CT_x material to realize the surface -O functional group modification of MXene, and used it as a negative electrode material in LIB [31]. Due to the increase in -O functional groups, the proportion of active sites increases, which in turn promotes the adsorption of Li^+ and improves the lithium-storage performance of electrode materials.

Herein, chemical exfoliation and low-temperature annealing methods were used to control the surface termination groups' surface end-capping groups of a few-layer $Ti_3C_2T_x$ nanosheet, which exhibited a reversible lithium-ion-storage specific capacity of 444.1 mAh g^{-1}. The increase in -O functional groups could increase the diffusion rate of Li^+, promote the transport of electrons, and accelerated the kinetics of the electrode reaction, thereby improving the performance of lithium-ion storage.

2. Materials and Methods

Preparation of $Ti_3C_2T_x$-F: The MAX phase (Ti_3AlC_2) was etched and stripped with HF solution to obtain two-dimensional layered $Ti_3C_2T_x$. A total of 0.83 g of Ti_3AlC_2 powder was slowly added to a polytetrafluoroethylene (PTFE) beaker filled with 20 mL of HF (40%) aqueous solution and stirred in a constant-temperature water bath at 60 °C for 2 h, centrifuged at 8000 rpm for 10 min, and washed multiple times with deionized water until the pH of the supernatant was 6–7. The washed production was put into a vacuum oven and dried at 80 °C for 24 h.

Preparation of $Ti_3C_2T_x$-T: a total of 0.5 g of $Ti_3C_2T_x$-F was dispersed in 5 mL of TMAOH solution and sonicated for 30 min, followed by magnetic stirring at 50 °C for 2 h and further ultrasonic treatment for 1 h to obtain the $Ti_3C_2T_x$-T material. The above

suspension was transferred to a dialysis bag (MD 44 mm), put into a beaker containing deionized water for dialysis treatment for 7 days, and the deionized water was changed regularly until the suspension in the dialysis bag became neutral. The resulting suspension was snap-frozen in liquid nitrogen and freeze-dried to obtain few-layer $Ti_3C_2T_x$.

Preparation of $Ti_3C_2T_x$-T(O): The surface modification of the few-layer $Ti_3C_2T_x$-T material was carried out by low-temperature annealing. In brief, 0.5 g of $Ti_3C_2T_x$-T material was heated to 280 °C for 2 h with a heating rate of 5 min^{-1} in tube furnace to obtain $Ti_3C_2T_x$-T(O). The schematic illustration for the preparation of $Ti_3C_2T_x$-T(O) is described in Scheme 1.

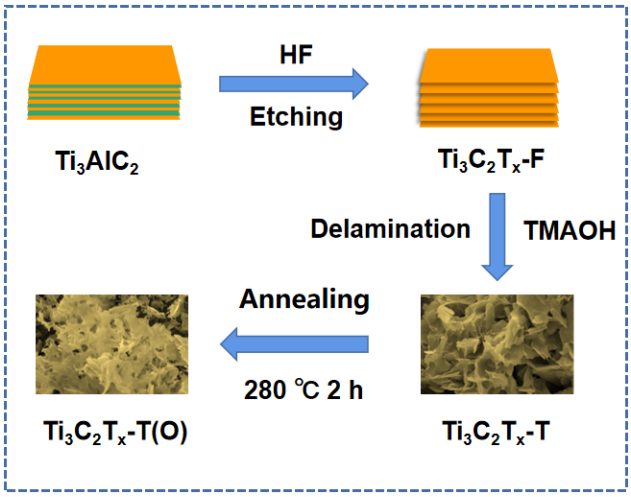

Scheme 1. The schematic illustration for the preparation of $Ti_3C_2T_x$-T(O).

The surface morphologies and microstructures of the samples were observed by SEM (Quanta FEG, USA), TEM and HRTEM (FEI Talos F200X, USA). XRD (ARL Equinox 3000 using Cu $K_{\alpha 1}$ radiation, USA) was used to measure the components and crystal structure. Raman (HORIBA JOBIN YVON S.A.S., France) spectroscopy was used to analyze the defect types and crystallinity of samples. Elemental chemical environment of the sample surface was analyzed by XPS (Thermo Scientific, ESCALAB 250 Xi, USA). FTIR spectra were recorded on PerkinElmer TL9000 (Canada) using KBr disks. The galvanostatic intermittent titration technique (GITT) was performed at a current density of 0.05 A g^{-1}. The specific surface area and pore-size distribution were measured by nitrogen absorption and desorption method on Microtrac BEL (Japan).

The samples were tested for electrochemical performance by LIBs. A total of 80 mg of the prepared material, 10 mg of acetylene black and 10 mg of polyvinylidene fluoride (PVDF) binder were weighed according to the mass ratio of 8:1:1, and then put into an agate mortar and fully ground for 30 min to obtain a uniformly dispersed slurry. The obtained slurry was coated on copper foil, scraped with a 200 μm scraper until the surface was uniform, transferred to a vacuum oven, and dried at 80 °C for 12 h. When the oven temperature dropped to room temperature, the copper foil was cut into circular electrode pieces with a diameter of 12 mm using a microtome, and the active material loading was about 1.15 mg cm^{-2}. In this paper, lithium foil was used as the counter electrode to assemble a CR2032 button battery case in a glove box filled with high-purity argon gas, and its electrochemical performance was tested. The liquid electrolyte was 1.0 M $LiPF_6$ in a mixture of ethylene carbonate (EC)/diethyl carbonate (DEC) with a volume ratio of 1:1, and the separator was a microporous membrane (Celgard2400). Constant current charge/discharge performance tests (cycling performance and rate performance) were performed by an automatic battery-tester system (Land CT2001A, China) at a constant temperature of 25 °C in a voltage range of 0.01 V to 3.0 V. Cyclic voltammetry (CV) tests were performed on a potential window range of 0 to 3.0 V at scan rates from 0.1 mV s^{-1} to 2 mV s^{-1} used a CHI760E (CH Instruments, China) electrochemical workstation. Elec-

trochemical impedance spectroscopy (EIS) was performed on a CHI760E electrochemical workstation with a test frequency range of 0.01 Hz to 1 MHz. The galvanostatic intermittent titration technique (GITT) was performed on an automatic battery-tester system (Land CT2001A, China) with a voltage range of 0.01 V~3.0 V (vs. Li/Li^+), a current density of 50 mA g^{-1}, a pulse of 5 min, and a relaxation of 55 min.

3. Results and Discussion

As shown in Figure 1a, the SEM image showed that $Ti_3C_2T_x$-F had a graphene-like layered structure, and its sheets were arranged in parallel in an accordion shape. As shown in Figure 1b, the few-layer $Ti_3C_2T_x$-T material prepared by exfoliating the layered $Ti_3C_2T_x$-F by TMAOH organic reagent showed the morphology of tightly stacked nanosheets, indicated that the layered $Ti_3C_2T_x$-F material was formed by the TMAOH organic reagent. It was peeled off into a few layers of $Ti_3C_2T_x$-T material, and the surface was relatively complete. As shown in Figure 1c,d, after low-temperature annealing, the edges of $Ti_3C_2T_x$-T(O) nanosheets were wrinkled and slightly curled to form a 3D network structure. It was found that the exfoliated MXene sheets maintain the diameter of the pristine MAX sheets in the size of ~10 μm.

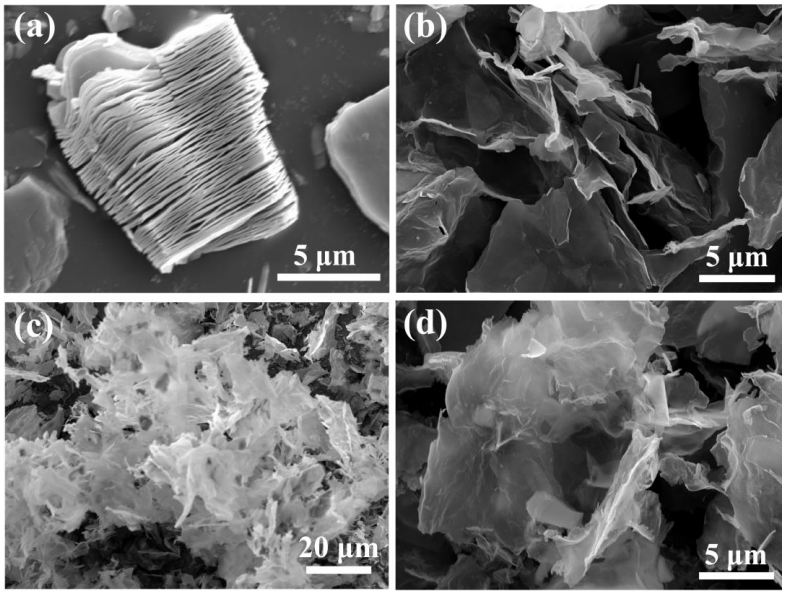

Figure 1. SEM images of (**a**) $Ti_3C_2T_x$-F; (**b**) $Ti_3C_2T_x$-T; (**c**) and (**d**) $Ti_3C_2T_x$-T(O).

In order to explore the microstructure on the surface of $Ti_3C_2T_x$-T(O) nanosheets, $Ti_3C_2T_x$-T(O) was tested by TEM. As shown in Figure 2a,b, $Ti_3C_2T_x$-T(O) nanosheets were thin and transparent, with wrinkles on the surface and edges, relatively complete morphology, no obvious defects, and oxide particles, indicating that the successful preparation had larger-size nanosheets with fewer defects. The EDS-mapping images showed that C, F, O, and Ti elements were uniformly distributed in the $Ti_3C_2T_x$-T(O) nanosheets.

The crystal phase structures of the above three materials were analyzed and tested by XRD, as shown in Figure 3a. After HF etching, the characteristic peak at 39° of the Ti_3AlC_2 raw material (JCPDS No 52-0875) almost disappeared, confirming that the Al atomic layer was removed from Ti_3AlC_2. The characteristic peaks at 9°, 18°, and 27° of $Ti_3C_2T_x$-F obtained by HF etching and lift-off corresponded to (002), (004), and (006) crystal planes, respectively [32]. The intensity of the diffraction peak of the high Miller index crystal plane of the $Ti_3C_2T_x$-T material obtained by TMAOH organic reagent for secondary exfoliation decreases, indicating that the multilayer $Ti_3C_2T_x$-F was fully exfoliated to obtain a few layers of $Ti_3C_2T_x$-T. The (002) characteristic peak intensity of the $Ti_3C_2T_x$-T(O) material obtained by low-temperature annealing treatment was weakened, indicating that the

material had certain wrinkles and curls, which was consistent with the results observed in SEM.

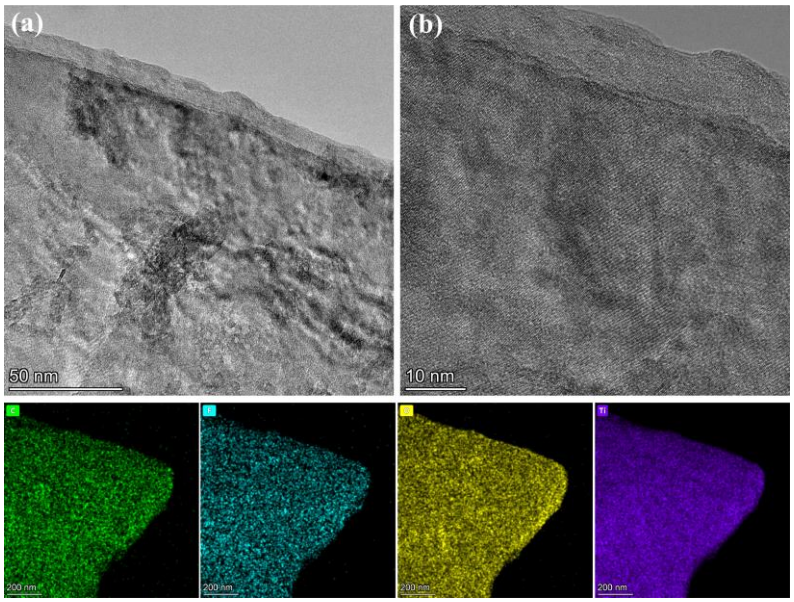

Figure 2. Microstructure characterizations of the $Ti_3C_2T_x$-T(O). (**a**) TEM image; (**b**) HRTEM image and the elemental EDS-mapping images of C, F, O, and Ti elements.

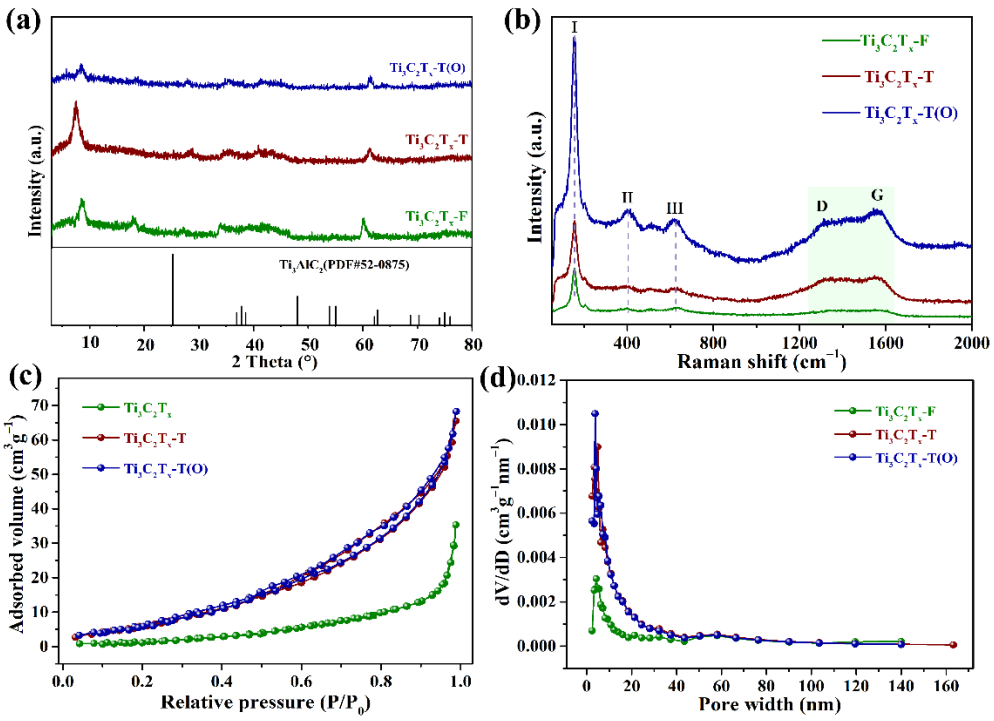

Figure 3. (**a**) XRD patterns; (**b**) Raman spectra; (**c**) N_2 adsorption/desorption isotherms; (**d**) the pore-size distribution of $Ti_3C_2T_x$-F, $Ti_3C_2T_x$-T and $Ti_3C_2T_x$-T(O).

In order to explore the molecular-structure information of the surface of $Ti_3C_2T_x$ material before and after modification, Raman spectroscopy was used to explore the material. As shown in Figure 3b, the characteristic peak I corresponded to the vibration of Ti–O or Ti–OH bonds (152.6 cm^{-1}), confirming that the surface contains $Ti_3C_2O_x$ and $Ti_3C_2(OH)_x$ compounds. The characteristic peaks of II and III corresponded to the stretching vibrations of Ti–C bonds (401.5 cm^{-1} and 606.2 cm^{-1}) [33]. There were two characteristic

peaks, D peak and G peak, at 1313.7 cm^{-1} and 1567.2 cm^{-1}, respectively. The D peak was caused by the deformation vibration of amorphous carbon or six-membered ring, and the G peak was caused by the stacking of graphite hexagonal network planes. After low-temperature annealing, the intensities of D peak and G peak of $Ti_3C_2T_x$-T(O) material increased, indicating that the carbon content of the material increased. After the micro-oxidation treatment, the Ti atomic layer in $Ti_3C_2T_x$ was destroyed, exposing more C atoms, which resulted in a slightly higher intensity of the G peak than that of the D peak [34].

Figure 3c,d showed the specific surface area and pore-size-distribution curves of the anode of $Ti_3C_2T_x$-F, $Ti_3C_2T_x$-T, and $Ti_3C_2T_x$-T(O), respectively. As shown in Figure 3c, the specific surface areas of $Ti_3C_2T_x$-F, $Ti_3C_2T_x$-T and $Ti_3C_2T_x$-T(O) can be calculated by BET theory to be 7.69 m^2 g^{-1}, 41.209 m^2 g^{-1} and 44.165 m^2 g^{-1}, respectively. As shown in Figure 3d, the pore sizes of $Ti_3C_2T_x$-F, $Ti_3C_2T_x$-T, and $Ti_3C_2T_x$-T(O) materials were calculated using the BJH model to ~0.013 cm^3 g^{-1}, ~0.101 cm^3 g^{-1} and ~0.106 cm^3 g^{-1}, respectively. Comparing the obtained data, it can be seen that the specific surface area of the sample showed a gradual trend of increasing, while the pore size showed a trend of first being larger and then smaller. The trend of sample porosity was basically consistent with the trend of the specific surface area of the sample.

To explore the elemental chemical environment on the material surface, XPS analysis was performed on $Ti_3C_2T_x$-F and $Ti_3C_2T_x$-T(O) materials. As shown in Figure 4a,d, the characteristic peaks located at 281.8, 284.8, 286.3, and 288.5 eV in the C 1*s* XPS spectrum correspond to C–Ti–O, C–C, C–OH and O–C=O bonds [35]. In the O 1*s* XPS spectra, 529.8, 531.6 and 533.0 eV correspond to Ti–O, Ti–OH and H_2O [36], respectively (shown in Figure 4b,e). As shown in Figure 4c,f, four pairs of double peaks (Ti $2p_{3/2}$ and Ti $2p_{1/2}$) could be obtained by fitting the Ti 2*p* XPS spectra, and each pair of peaks conforms to a fixed area ratio (2:1) and a fixed peak spacing (5.7 eV). The peaks at binding energies of 454.8 and 455.8 eV in Ti $2p_{3/2}$ correspond to Ti–C and Ti–F bonds, and the peaks at binding energies of 457.0 and 458.6 eV correspond to Ti–O bonds (Ti^{3+}:Ti_xO_y, Ti^{4+}:TiO_2). Compared with Ti 2*p* in $Ti_3C_2T_x$-F, Ti 2*p* in $Ti_3C_2T_x$-T(O) had reduced the characteristic peak intensity of Ti–C at 454.8 eV and Ti–F at 455.8 eV, and enhanced the Ti–O characteristic peak intensity at 458.6 eV [37]. The quantitative analysis of the sample surface by XPS indicated that the proportion of oxygen atoms of $Ti_3C_2T_x$-F was 18.04 at.%; the proportion of fluorine atoms was 12.74 at.%. In addition, the proportion of oxygen atoms of $Ti_3C_2T_x$-T(O) was 44.15 at.%, and the proportion of fluorine atoms was 1.72 at.%. The above phenomenon showed that the relative content of Ti–O on the surface of the material increased and the relative content of Ti–F decreased after low-temperature annealing treatment. Oxygen substitution occurred after the Ti–F bond was oxidized, and the content of oxygen-containing functional groups on the surface of the material increased.

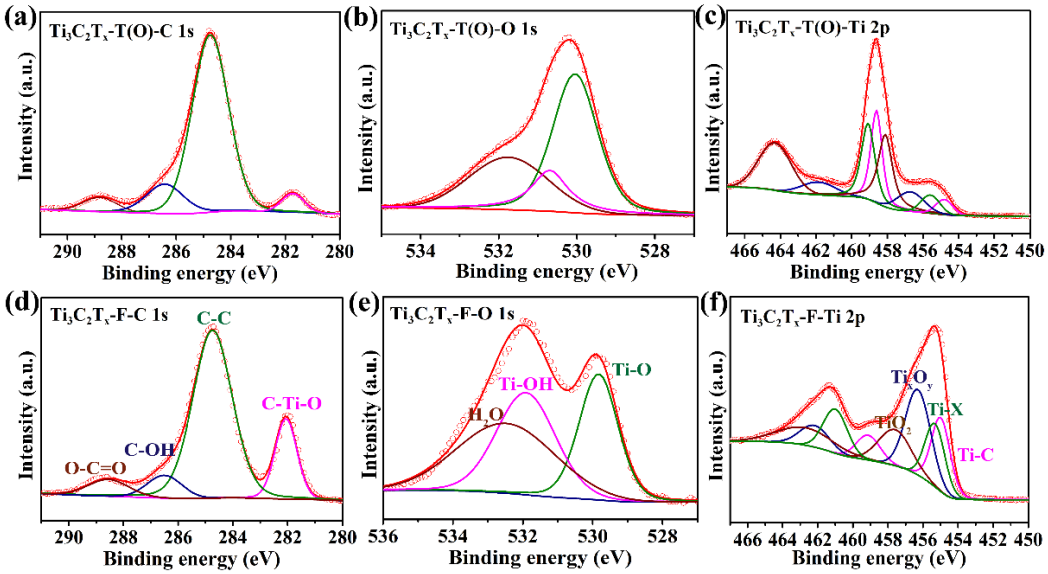

Figure 4. XPS spectra for high-resolution (**a**,**d**) C 1*s*; (**b**,**e**) O 1*s*; (**c**,**f**) Ti 2*p* of $Ti_3C_2T_x$-T(O) and $Ti_3C_2T_x$-F.

Figure 5a showed the constant current charge–discharge curve of $Ti_3C_2T_x$-T(O) negative electrode in the voltage range of 0.01 V–3.0 V. Under the current density of 0.1 A g^{-1}, the discharge-specific capacity of the first cycle was 650.41 mAh g^{-1}, the charge-specific capacity of the first cycle was 406.87 mAh g^{-1}, and the corresponding initial coulomb efficiency (ICE) was 62.56%. The voltage plateau at 0.8 V in the first cycle of the discharge curve corresponds to the formation of the SEI (solid electrolyte interface) film in the first cycle. The charge–discharge curves of the 2nd, 50th, and 100th cycles basically coincide, which proved that the material had good cycle stability.

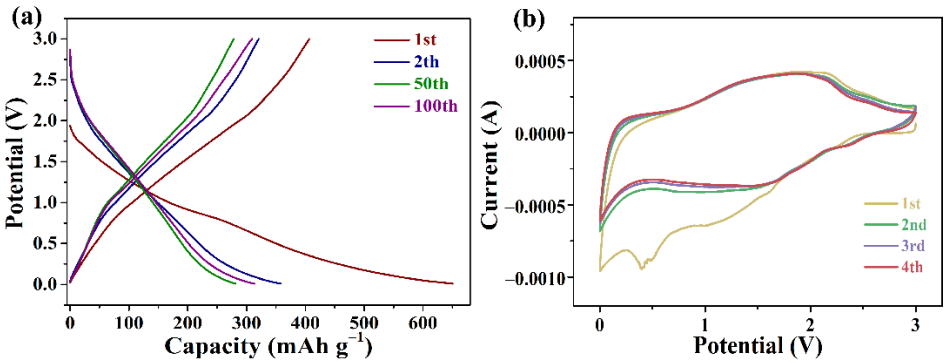

Figure 5. (**a**) Charge/discharge profiles at 0.1 A g^{-1} of $Ti_3C_2T_x$-T(O) anode; (**b**) CV curves at a scan rate of 2 mV s^{-1}.

In order to study the electrochemical kinetic process of $Ti_3C_2T_x$-T(O) anode, EIS test was carried out. The Nyquist curve consisted of a semicircle in the high- to mid-frequency region and a sloping line in the low-frequency region. The semicircle represented the charge-transfer resistance (R_{ct}) of the electrode and the electric double-layer capacitance (CPE) with capacitive properties, and the oblique line corresponds to the diffusion resistance (Z_w) of lithium ions in the electrolyte. The intercept in the high-frequency region on the Z′ axis represented the contact resistance (R_s) between the electrode and the electrolyte [38]. As shown in Figure 6a, the R_{ct} values of $Ti_3C_2T_x$-F, $Ti_3C_2T_x$-T and $Ti_3C_2T_x$-T(O) anodes were 506.8, 202.5 and 89.1 Ω, respectively, indicating that $Ti_3C_2T_x$-T(O) anodes had good charge-transfer kinetic characteristics and good conductivity.

As shown in Figure 6b, at the current densities of 0.1, 0.2, 0.5, 1, 2, and 5 A g^{-1}, the discharge-specific capacities of the $Ti_3C_2T_x$-T(O) anode were 285.2, 228.6, 209.2, 188.9, 174.4, and 151.4 mAh g^{-1}. When the current density returned to a small current density of 0.1 A g^{-1}, the discharge capacity of the $Ti_3C_2T_x$-T(O) anode recovered to 265.2 mAh g^{-1}, indicating that the material had good reversibility. In contrast, the specific discharge capacities of $Ti_3C_2T_x$-F electrodes at current densities of 0.1, 0.2, 0.5, 1, 2, 5, and 0.1 A g^{-1} were only 193.5, 118.4, 94.5, 75.0, 58.3, 43.1, and 124.9 mAh g^{-1}. Compared with the $Ti_3C_2T_x$-F electrode, the $Ti_3C_2T_x$-T(O) electrode had better rate performance, because the few-layer structure can effectively shorten the ion-diffusion path and improve the diffusion rate; the specific surface area increased, the oxygen-containing functional groups on the surface increased, the proportion of active sites increased, and the reaction kinetics was promoted.

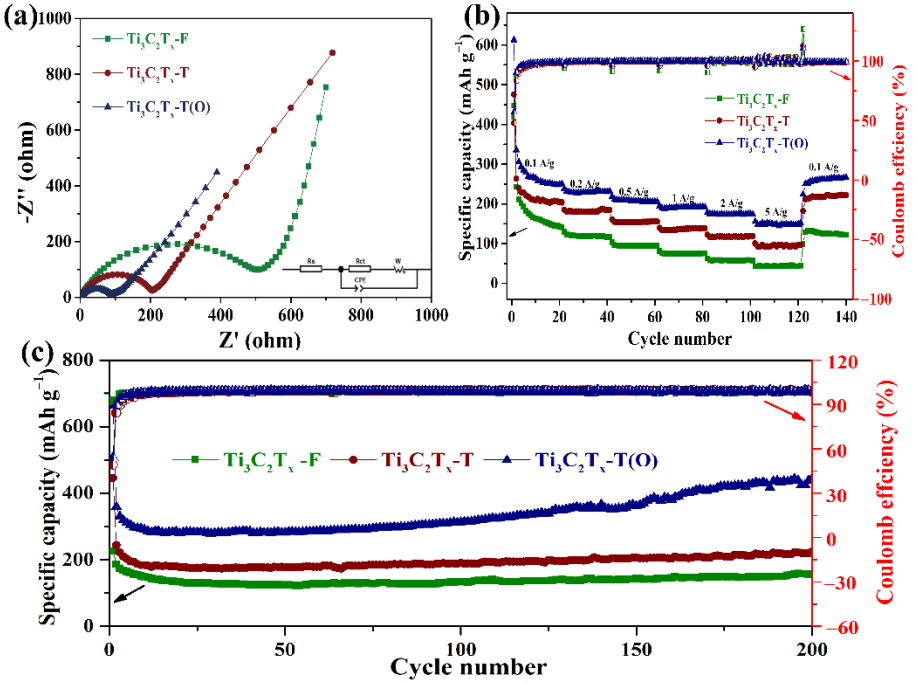

Figure 6. (**a**) Nyquist plots; (**b**) rate performance at different current densities; (**c**) cycling performance at 0.1 A g^{-1} for different anodes of $Ti_3C_2T_x$-F, $Ti_3C_2T_x$-T and $Ti_3C_2T_x$-T(O).

As shown in Figure 6c, the initial discharge-specific capacities of the $Ti_3C_2T_x$-F, $Ti_3C_2T_x$-T, and $Ti_3C_2T_x$-T(O) anodes were 226.2, 444.9, and 665 mAh g^{-1}, respectively. The ICE of $Ti_3C_2T_x$-T anode was 49.15 %, and the ICE of the $Ti_3C_2T_x$-T(O) anode after oxidation treatment was 53.75 %. The improvement of ICE might be related to the substitution of -F functional groups on the surface by -O functional groups. After 200 cycles, the $Ti_3C_2T_x$-T(O) anode exhibited a specific discharge capacity of 444.1 mAh g^{-1} and a capacity retention rate of 124.05 %. In contrast, the $Ti_3C_2T_x$-T anode had a specific discharge capacity of 224.8 mAh g^{-1} after 200 cycles, and a capacity retention rate of only 92.21 %. According to the analysis of physicochemical properties/electrochemical lithium-storage performance, the improved electrochemical cycling stability of $Ti_3C_2T_x$-T(O) was closely related to the substitution of -O functional groups for -F functional groups on the surface of $Ti_3C_2T_x$-T, in which a large number of oxygen-containing functional groups could provide more energy for Li^+ more active sites, thereby improving the lithium-storage performance of the electrode. The $Ti_3C_2T_x$-T(O) negative electrode exhibited a phenomenon of "negative growth" (capacity first decreases and then increases) during the cycle. It was speculated that the repeated deintercalation of Li^+ between the $Ti_3C_2T_x$-T(O) layers during the cycle causes the interlayer spacing to increase. The chemically active lithium-storage sites were continuously activated, resulting in an increase in the pseudocapacitance contribution of

the electrode surface. In future work, the following methods could be used to improve the ICE of the electrode: short-circuiting the negative pole piece by electrical contact with the short-circuit method, adjusting the resistance and processing time of the short-circuit wire, and realizing prelithiation under the action of the potential difference; using lithium-aromatic compounds (lithium naphthalene, butyllithium) to immerse or spray the negative electrode material to achieve chemical prelithiation [39,40]; functionally modifying the metal electrode with the help of artificial SEI layer technology to improve the ICE [41].

To investigate the Li^+ diffusion kinetics of $Ti_3C_2T_x$-F, $Ti_3C_2T_x$-T and $Ti_3C_2T_x$-T(O) anodes, GITT measurements were performed at a current density of 0.05 A g^{-1}, and the pulse and relaxation processes are shown in Figure 7a. First, a current was applied to the pulse, and the battery potential raised rapidly during the pulse. Subsequently, the charging current was kept constant, and the potential was slowly raised. Finally, entering the relaxation process, the composition in the electrode tended to be homogeneous through Li^+ diffusion, and the potential decreased slowly until it equilibrated again. Compared with $Ti_3C_2T_x$-F and $Ti_3C_2T_x$-T, $Ti_3C_2T_x$-T(O) anode exhibited smaller overpotentials during charging, indicating a better diffusion rate. The diffusion coefficients D of $Ti_3C_2T_x$-F, $Ti_3C_2T_x$-T, and $Ti_3C_2T_x$-T(O) electrodes changed periodically with the lithiation process (Corresponding to the discharge process of Figure 7a), and the maximum diffusion rates were 1.12×10^{-11} cm^2 s^{-1}, 3.94×10^{-11} cm^2 s^{-1} and 5.76×10^{-11} cm^2 s^{-1} (Figure 7b). The Li^+ diffusion coefficients of the $Ti_3C_2T_x$-T(O) electrode at each potential were higher than those of the two, which was related to the increased oxygen-containing functional groups in the surface modification of the material. The replacement of some -F functional groups on the surface by -O functional groups could improve the diffusion rate of Li^+, optimize the electron/ion transport pathway, and accelerate the kinetics of the electrode reaction, thereby enhancing the cycling stability and rate capability.

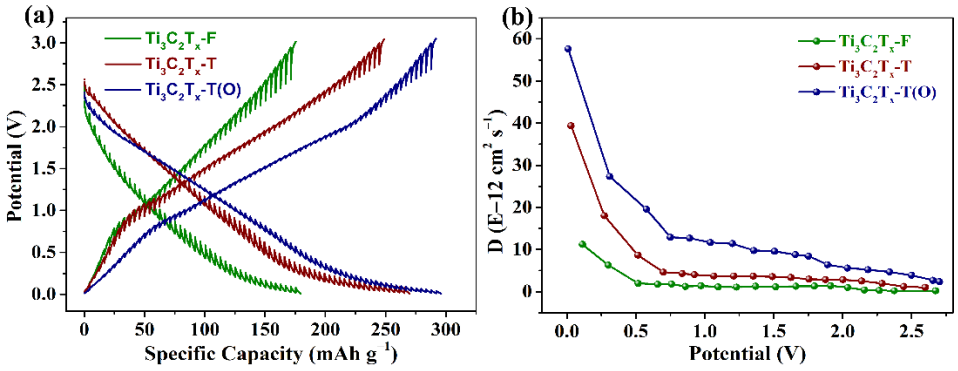

Figure 7. (**a**) GITT results and (**b**) diffusion coefficient for $Ti_3C_2T_x$-F, $Ti_3C_2T_x$-T, and $Ti_3C_2T_x$-T(O) anodes at different potentials.

By studying the CV curves of the $Ti_3C_2T_x$-T(O) anode at different scanning speeds, the kinetics of lithium storage was explored and the contribution ratio of capacitance was calculated. Figure 8a shows the CV curves of the $Ti_3C_2T_x$-T(O) anode at different scan rates. According to the cyclic voltammetry test formula $i = av^b$, it was logarithmically transformed to obtain $\log(i) = b\log(v) + \log(a)$. The b value of the redox peak of the electrode was calculated by plotting the $\log(i)$-$\log(v)$ curve. When $b = 0.5$, it indicated that the electrode reaction was dominated by diffusion, and when $b = 1$, it indicated that the electrode reaction was dominated by surface pseudocapacitance as host [42]. As shown in Figure 8b, the b values of the oxidation peak (~1.5 V) and reduction peak (~1.7 V) of the $Ti_3C_2T_x$-T(O) anode were calculated to be 0.76 and 0.77, respectively. The total capacity of the electrode was divided into two parts: (1) the capacity contribution provided by the ion-diffusion process; (2) the pseudocapacitive contribution provided by the redox reaction that occurs during the charge-transfer process on the electrode surface. The lithium storage form of the $Ti_3C_2T_x$-T(O) anode was quantified, as shown in Figure 8c. At the scan rate of 0.1 mV s^{-1},

the capacitive contribution of the negative electrode of $Ti_3C_2T_x$-T(O) accounted for 23.14%, and when the scan rate increased to 1.0 mV s^{-1}, the capacitive contribution increased to 69.75%. With the increase, the diffusion rate of Li^+ at the electrode interface was accelerated, and the pseudocapacitance contribution increased.

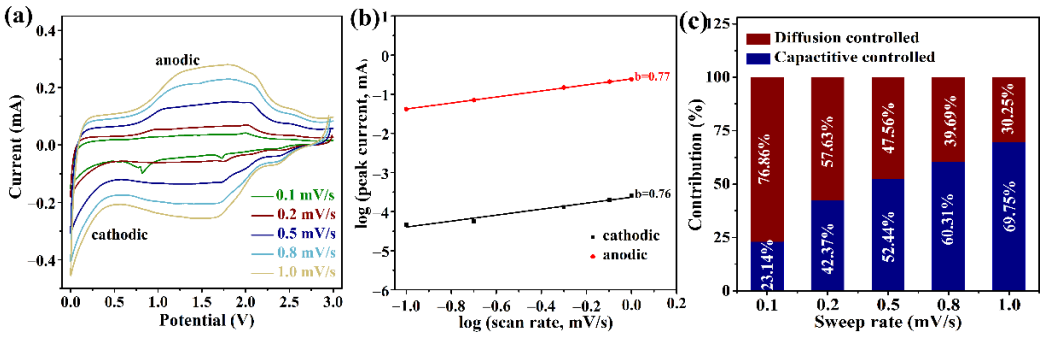

Figure 8. (**a**) CV profiles at different sweep rates; (**b**) relationship between log(*i*) *vs* log(*v*); and (**c**) contribution ratio of capacities at different sweep rates for the $Ti_3C_2T_x$-T(O) anodes.

4. Conclusions

In summary, few-layer $Ti_3C_2T_x$-T(O) anode materials with rich -O functional groups on the surface were successfully prepared by HF etching of MAX phase, few-layer stripping of TMAOH organic reagents, and low-temperature oxidation. The micro-oxidation annealing treatment caused some fluorine end-groups on the surface to be replaced by oxygen end-groups, which optimizes the types of end-groups on the surface of the material. The $Ti_3C_2T_x$-T(O) anode exhibited a reversible capacity of 444.1 mAh g^{-1} after 200 cycles at a current density of 0.1 A g^{-1} and a reversible capacity of 174.4 mAh g^{-1} at a large current density of 5 A g^{-1}. The increased of -O functional groups on the surface of $Ti_3C_2T_x$-T(O) material accelerated the diffusion rate of Li^+, optimized the electron-/ion-transport pathway, and accelerated the kinetics of the electrode reaction. The $Ti_3C_2T_x$-T(O) nanosheets were folded and curled to form a network structure, which increased the active sites and shortened the Li^+ transport path.

Author Contributions: Conceptualization, A.L. and X.W.; methodology, X.W.; writing—original draft preparation, A.L.; writing—review and editing, C.D. and D.W.; supervision, J.C. and Z.M. All authors have read and agreed to the published version of the manuscript.

Funding: This research was funded by the financial support of National Natural Science Foundation of China (Grant No. 51777138) and Scientific Developing Foundation of Tianjin Education Commission (Grant No. 2018ZD09).

Institutional Review Board Statement: Not applicable.

Informed Consent Statement: Not applicable.

Data Availability Statement: Not applicable.

Conflicts of Interest: The authors declare no conflict of interest.

References

1. Pang, J.B.; Mendes, R.G.; Bachmatiuk, A.; Zhao, L.; Ta, H.Q.; Gemming, T.; Liu, H.; Liu, Z.F.; Rummeli, M.H. Applications of 2D MXenes in energy conversion and storage systems. *Chem. Soc. Rev.* **2019**, *48*, 72–133. [CrossRef] [PubMed]
2. Aslam, M.K.; Niu, Y.B.; Xu, M.W. MXenes for Non-Lithium-Ion (Na, K, Ca, Mg, and Al) Batteries and Supercapacitors. *Adv. Energy Mater.* **2021**, *11*, 2000681. [CrossRef]
3. Wang, Y.G.; Song, Y.F.; Xia, Y.Y. Electrochemical capacitors: Mechanism, materials, systems, characterization and applications. *Chem. Soc. Rev.* **2016**, *45*, 5925–5950. [CrossRef] [PubMed]
4. Zhang, P.P.; Wang, F.X.; Yu, M.H.; Zhuang, X.D.; Feng, X.L. Two-dimensional materials for miniaturized energy storage devices: From individual devices to smart integrated systems. *Chem. Soc. Rev.* **2018**, *47*, 7426–7451. [CrossRef]

5. Liu, Y.T.; Zhu, X.D.; Pan, L. Hybrid Architectures based on 2D MXenes and Low-Dimensional Inorganic Nanostructures: Methods, Synergies, and Energy-Related Applications. *Small* **2018**, *14*, 201803632. [CrossRef]
6. Alhabeb, M.; Maleski, K.; Anasori, B.; Lelyukh, P.; Clark, L.; Sin, S.; Gogotsi, Y. Guidelines for Synthesis and Processing of Two-Dimensional Titanium Carbide (Ti_3C_2TX MXene). *Chem. Mater.* **2017**, *29*, 7633–7644. [CrossRef]
7. Anasori, B.; Lukatskaya, M.R.; Gogotsi, Y. 2D metal carbides and nitrides (MXenes) for energy storage. *Nat. Rev. Mater.* **2017**, *2*, 17. [CrossRef]
8. Anasori, B.; Xie, Y.; Beidaghi, M.; Lu, J.; Hosler, B.C.; Hultman, L.; Kent, P.R.C.; Gogotsi, Y.; Barsoum, M.W. Two-Dimensional, Ordered, Double Transition Metals Carbides (MXenes). *ACS Nano* **2015**, *9*, 9507–9516. [CrossRef]
9. Naguib, M.; Kurtoglu, M.; Presser, V.; Lu, J.; Niu, J.J.; Heon, M.; Hultman, L.; Gogotsi, Y.; Barsoum, M.W. Two-Dimensional Nanocrystals Produced by Exfoliation of Ti3AlC2. *Adv. Mater.* **2011**, *23*, 4248–4253. [CrossRef]
10. Naguib, M.; Mashtalir, O.; Carle, J.; Presser, V.; Lu, J.; Hultman, L.; Gogotsi, Y.; Barsoum, M.W. Two-Dimensional Transition Metal Carbides. *ACS Nano* **2012**, *6*, 1322–1331. [CrossRef]
11. Shahzad, F.; Alhabeb, M.; Hatter, C.B.; Anasori, B.; Hong, S.M.; Koo, C.M.; Gogotsi, Y. Electromagnetic interference shielding with 2D transition metal carbides (MXenes). *Science* **2016**, *353*, 1137–1140. [CrossRef] [PubMed]
12. Zhang, X.; Zhang, Z.H.; Zhou, Z. MXene-based materials for electrochemical energy storage. *J. Energy Chem.* **2018**, *27*, 73–85. [CrossRef]
13. Ghidiu, M.; Naguib, M.; Shi, C.; Mashtalir, O.; Pan, L.M.; Zhang, B.; Yang, J.; Gogotsi, Y.; Billinge, S.J.L.; Barsoum, M.W. Synthesis and characterization of two-dimensional Nb_4C_3 (MXene). *Chem. Commun.* **2014**, *50*, 9517–9520. [CrossRef] [PubMed]
14. Ng, V.M.H.; Huang, H.; Zhou, K.; Lee, P.S.; Que, W.X.; Xu, Z.C.J.; Kong, L.B. Recent progress in layered transition metal carbides and/or nitrides (MXenes) and their composites: Synthesis and applications. *J. Mater. Chem. A* **2017**, *5*, 8769.
15. Mashtalir, O.; Lukatskaya, M.R.; Zhao, M.Q.; Barsoum, M.W.; Gogotsi, Y. Amine-Assisted Delamination of Nb2C MXene for Li-Ion Energy Storage Devices. *Adv. Mater.* **2015**, *27*, 3501–3506. [CrossRef]
16. Mashtalir, O.; Naguib, M.; Mochalin, V.N.; Dall'Agnese, Y.; Heon, M.; Barsoum, M.W.; Gogotsi, Y. Intercalation and delamination of layered carbides and carbonitrides. *Nat. Commun.* **2013**, *4*, 1716–1723. [CrossRef] [PubMed]
17. Soundiraraju, B.; George, B.K. Two-Dimensional Titanium Nitride (Ti_2N) MXene: Synthesis, Characterization, and Potential Application as Surface-Enhanced Raman Scattering Substrate. *ACS Nano* **2017**, *11*, 8892–8900. [CrossRef] [PubMed]
18. Bak, S.M.; Qiao, R.M.; Yang, W.L.; Lee, S.; Yu, X.Q.; Anasori, B.; Lee, H.; Gogotsi, Y.; Yang, X.Q. Na-Ion Intercalation and Charge Storage Mechanism in 2D Vanadium Carbide. *Adv. Energy Mater.* **2017**, *7*, 1700959. [CrossRef]
19. Kim, S.J.; Naguib, M.; Zhao, M.Q.; Zhang, C.F.; Jung, H.T.; Barsoum, M.W.; Gogotsi, Y. High mass loading, binder-free MXene anodes for high areal capacity Li-ion batteries. *Electrochim. Acta* **2015**, *163*, 246–251. [CrossRef]
20. Sun, D.D.; Wang, M.S.; Li, Z.Y.; Fan, G.X.; Fan, L.Z.; Zhou, A.G. Two-dimensional Ti_3C_2 as anode material for Li-ion batteries. *Electrochem. Commun.* **2014**, *47*, 80–83. [CrossRef]
21. Liang, X.Y.; Yan, L.J.; Li, W.P.; Bai, Y.C.; Zhu, C.; Qiang, Y.J.; Xiong, B.X.; Xiang, B.; Zou, X.F. Flexible high-energy and stable rechargeable vanadium-zinc battery based on oxygen defect modulated V_2O_5 cathode. *Nano Energy* **2021**, *87*, 106164. [CrossRef]
22. Lukatskaya, M.R.; Kota, S.; Lin, Z.F.; Zhao, M.Q.; Shpigel, N.; Levi, M.D.; Halim, J.; Taberna, P.L.; Barsoum, M.; Simon, P.; et al. Ultra-high-rate pseudocapacitive energy storage in two-dimensional transition metal carbides. *Nat. Energy* **2017**, *2*, 17105. [CrossRef]
23. Okubo, M.; Sugahara, A.; Kajiyama, S.; Yamada, A. MXene as a Charge Storage Host. *Acc. Chem. Res.* **2018**, *51*, 591–599. [CrossRef] [PubMed]
24. Wang, X.; Kajiyama, S.; Iinuma, H.; Hosono, E.; Oro, S.; Moriguchi, I.; Okubo, M.; Yamada, A. Pseudocapacitance of MXene nanosheets for high-power sodium-ion hybrid capacitors. *Nat. Commun.* **2015**, *6*, 6544. [CrossRef]
25. Hart, J.L.; Hantanasirisakul, K.; Lang, A.C.; Anasori, B.; Pinto, D.; Pivak, Y.; van Omme, J.T.; May, S.J.; Gogotsi, Y.; Taheri, M.L. Control of MXenes' electronic properties through termination and intercalation. *Nat. Commun.* **2019**, *10*, 522. [CrossRef]
26. Khazaei, M.; Ranjbar, A.; Arai, M.; Yunoki, S. Topological insulators in the ordered double transition metals M-2′ M ″C-2 MXenes (M′ = Mo, W.; M′′ = Ti, Zr, Hf). *Phys. Rev. B* **2016**, *94*, 125152. [CrossRef]
27. Dong, Y.F.; Wu, Z.S.; Zheng, S.H.; Wang, X.H.; Qin, J.Q.; Wang, S.; Shi, X.Y.; Bao, X.H. Ti_3C_2 MXene-Derived Sodium/Potassium Titanate Nanoribbons for High-Performance Sodium/Potassium Ion Batteries with Enhanced Capacities. *ACS Nano* **2017**, *11*, 4792–4800. [CrossRef]
28. Hu, Q.K.; Sun, D.D.; Wu, Q.H.; Wang, H.Y.; Wang, L.B.; Liu, B.Z.; Zhou, A.G.; He, J.L. MXene: A New Family of Promising Hydrogen Storage Medium. *J. Phys. Chem. A* **2013**, *117*, 14253–14260. [CrossRef]
29. Tang, Q.; Zhou, Z.; Shen, P.W. Are MXenes Promising Anode Materials for Li Ion Batteries? Computational Studies on Electronic Properties and Li Storage Capability of Ti_3C_2 and $Ti_3C_2X_2$ (X = F, OH) Monolayer. *J. Am. Chem. Soc.* **2012**, *134*, 16909–16916. [CrossRef]
30. Lian, P.C.; Dong, Y.F.; Wu, Z.S.; Zheng, S.H.; Wang, X.H.; Wang, S.; Sun, C.L.; Qin, J.Q.; Shi, X.Y.; Bao, X.H. Alkalized Ti_3C_2 MXene nanoribbons with expanded interlayer spacing for high-capacity sodium and potassium ion batteries. *Nano Energy* **2017**, *40*, 1–8. [CrossRef]
31. Ahmed, B.; Anjum, D.H.; Hedhili, M.N.; Gogotsi, Y.; Alshareef, H.N. H_2O_2 assisted room temperature oxidation of Ti_2C MXene for Li-ion battery anodes. *Nanoscale* **2016**, *8*, 7580–7587. [CrossRef] [PubMed]

32. Wang, X.H.; Zhou, Y.C. Solid-liquid reaction synthesis of layered machinable Ti_3AlC_2 ceramic. *J. Mater. Chem.* **2002**, *12*, 455–460. [CrossRef]
33. Krishnamoorthy, K.; Pazhamalai, P.; Sahoo, S.; Kim, S.J. Titanium carbide sheet based high performance wire type solid state supercapacitors. *J. Mater. Chem. A* **2017**, *5*, 5726–5736. [CrossRef]
34. Tang, Y.; Zhu, J.F.; Yang, C.H.; Wang, F. Enhanced Capacitive Performance Based on Diverse Layered Structure of Two-Dimensional Ti_3C_2 MXene with Long Etching Time. *J. Electrochem. Soc.* **2016**, *163*, A1975–A1982. [CrossRef]
35. Rozmyslowska-Wojciechowska, A.; Wojciechowski, T.; Ziemkowska, W.; Chlubny, L.; Olszyna, A.; Jastrzebska, A.M. Surface interactions between 2D Ti_3C_2/Ti_2C MXenes and lysozyme. *Appl. Surf. Sci.* **2019**, *473*, 409–418. [CrossRef]
36. Pan, H.; Huang, X.X.; Zhang, R.; Wang, D.; Chen, Y.T.; Duan, X.M.; Wen, G.W. Titanium oxide-Ti_3C_2 hybrids as sulfur hosts in lithium-sulfur battery: Fast oxidation treatment and enhanced polysulfide adsorption ability. *Chem. Eng. J.* **2019**, *358*, 1253–1261. [CrossRef]
37. Rakhi, R.B.; Ahmed, B.; Hedhili, M.N.; Anjum, D.H.; Alshareef, H.N. Effect of Postetch Annealing Gas Composition on the Structural and Electrochemical Properties of Ti_2CTx MXene Electrodes for Supercapacitor Applications. *Chem. Mater.* **2015**, *27*, 5314–5323. [CrossRef]
38. Ahmed, B.; Anjum, D.H.; Gogotsi, Y.; Alshareef, H.N. Atomic layer deposition of SnO_2 on MXene for Li-ion battery anodes. *Nano Energy* **2017**, *34*, 249–256. [CrossRef]
39. Shen, Y.F.; Zhang, J.M.; Pu, Y.F.; Wang, H.; Wang, B.; Qian, J.F.; Cao, Y.L.; Zhong, F.P.; Ai, X.P.; Yang, H.X. Effective Chemical Prelithiation Strategy for Building a Silicon/Sulfur Li-Ion Battery. *ACS Energy Lett.* **2019**, *4*, 1717–1724. [CrossRef]
40. Choi, J.; Jeong, H.; Jang, J.; Jeon, A.R.; Kang, I.; Kwon, M.; Hong, J.; Lee, M. Weakly Solvating Solution Enables Chemical Prelithiation of Graphite–SiOx Anodes for High-Energy Li-Ion Batteries. *J. Am. Chem. Soc.* **2021**, *143*, 9169–9176. [CrossRef]
41. Zhao, F.F.; Zhai, P.B.; Wei, Y.; Yang, Z.L.; Chen, Q.; Zuo, J.H.; Gu, X.K.; Gong, Y.J. Constructing Artificial SEI Layer on Lithiophilic MXene Surface for High-Performance Lithium Metal Anodes. *Adv. Sci.* **2022**, *9*, 2103930. [CrossRef] [PubMed]
42. Wang, J.; Polleux, J.; Lim, J.; Dunn, B. Pseudocapacitive contributions to electrochemical energy storage in TiO_2 (anatase) nanoparticles. *J. Phys. Chem. C* **2007**, *111*, 14925–14931. [CrossRef]